The Astrophysical Journal Letters, 991:L40 (10pp), 2025 October 1 https://doi.org/10.3847/2041-8213/ae057a

The Light Echo of a High-redshift Quasar Mapped with Lyα Tomography

Anna-Christina Eilers[1,2], Minghao Yue[2], Jorryt Matthee[3], Joseph F. Hennawi[4,5], Frederick B. Davies[6], Robert A. Simcoe[1,2], Richard Teague[7], Rongmon Bordoloi[8], Gabriel Brammer[9], Yi Kang[5], Daichi Kashino[10], Ruari Mackenzie[11], Rohan P. Naidu[2], and Benjamín Navarrete[3]
[1] Department of Physics, Massachusetts Institute of Technology, Cambridge, MA 02139, USA; eilers@mit.edu
[2] MIT Kavli Institute for Astrophysics and Space Research, Massachusetts Institute of Technology, Cambridge, MA 02139, USA
[3] Institute of Science and Technology Austria (ISTA), Am Campus 1, 3400 Klosterneuburg, Austria
[4] Leiden Observatory, Leiden University, P.O. Box 9513, 2300 RA Leiden, The Netherlands
[5] Department of Physics, University of California, Santa Barbara, CA 93106-9530, USA
[6] Max-Planck-Institut für Astronomie, Königstuhl 17, D-69117 Heidelberg, Germany
[7] Department of Earth, Atmospheric, and Planetary Sciences, Massachusetts Institute of Technology, Cambridge, MA 02139, USA
[8] Department of Physics, North Carolina State University, Raleigh, NC 27695, USA
[9] Niels Bohr Institute, University of Copenhagen, Jagtvej 128, Copenhagen, Denmark
[10] National Astronomical Observatory of Japan, 2-21-1 Osawa, Mitaka, Tokyo 181-8588, Japan
[11] Department of Physics, ETH Zürich, Wolfgang-Pauli-Strasse 27, Zürich, 8093, Switzerland
Received 2025 August 22; revised 2025 September 5; accepted 2025 September 9; published 2025 September 25

Abstract

Ultraviolet (UV) radiation from accreting black holes ionizes the intergalactic gas around early quasars, carving out highly ionized bubbles in their surroundings. Any changes in a quasar's luminosity are therefore predicted to produce outward-propagating ionization gradients, affecting the Lyα absorption opacity near the quasar's systemic redshift. This "proximity effect" is well-documented in rest-UV quasar spectra but only provides a one-dimensional probe along our line of sight. Here we present deep spectroscopic observations with the James Webb Space Telescope (JWST) of galaxies in the background of a superluminous quasar at $z_{\rm QSO} \approx 6.3$, which reveal the quasar's "light echo" with Lyα tomography in the transverse direction. This transverse proximity effect is detected for the first time toward multiple galaxy sightlines, allowing us to map the extent and geometry of the quasar's ionization cone. We obtain constraints on the orientation and inclination of the cone, as well as an upper limit on the obscured solid angle fraction of $f_{\rm obsc} < 91\%$. Additionally, we find a timescale of the quasar's UV radiation of $t_{\rm QSO} = 10^{5.6^{+0.1}_{-0.3}}$ yr, which is significantly shorter than would be required to build up the central supermassive black hole (SMBH) with conventional growth models, but is consistent with independent measurements of the quasars' duty cycle. Our inferred obscured fraction disfavors a scenario where short quasar lifetimes can be explained exclusively by geometric obscuration, and instead supports the idea that radiatively inefficient accretion or growth in initially heavily enshrouded cocoons plays a pivotal role in early SMBH growth. Our results pave the way for novel studies of quasars' ionizing geometries and radiative histories at early cosmic times.

Unified Astronomy Thesaurus concepts: Quasars (1319); Supermassive black holes (1663); Early universe (435)

1. Introduction

Supermassive black holes (SMBHs) reside at the heart of every massive galaxy, regulating the evolution of their hosts, injecting energy into the circum- and intergalactic media (IGM), and shaping entire galactic ecosystems over cosmic time. Yet the formation and growth of these SMBHs, in particular at early cosmic times, is still highly debated. At redshift $z \gtrsim 6$, the timescale required to grow a billion solar mass black hole is comparable to the age of the Universe when assuming a canonical value for the radiative efficiency of $\epsilon \approx 10\%$ for the standard thin accretion disk theory in general relativity (N. I. Shakura & R. A. Sunyaev 1973; T. Tanaka & Z. Haiman 2009; K. Inayoshi et al. 2020), which has led many studies to invoke massive initial black hole seeds in excess of stellar remnants (M. C. Begelman et al. 2006), or suggest rapid, radiatively inefficient accretion episodes (e.g., K. Inayoshi et al. 2016; M. C. Begelman & M. Volonteri 2017).

Since the luminosity of quasars is powered by accretion onto their central SMBHs (A. Soltan 1982; Q. Yu & S. Tremaine 2002), we can chronicle the black hole growth by studying the radiative histories of quasars. The quasars' ionizing radiation alters the ionization state of the surrounding intergalactic gas, resulting in a decrease in the opacity to Lyα photons, which is known as the "proximity effect." This effect is well-documented in rest-UV quasar spectra along our line of sight (X. Fan et al. 2006; C. L. Carilli et al. 2010; A.-C. Eilers et al. 2017, 2020; K. A. Morey et al. 2021; S. Satyavolu et al. 2023a), but should also be observable in the transverse direction observed in absorption spectra of background sources intersecting the environment of an ionizing source at close projected distances (K. L. Adelberger 2004; E. Visbal & R. A. C. Croft 2008; T. M. Schmidt et al. 2019). Due to the finite speed of light c, the transverse direction of the proximity effect is sensitive to the quasar's radiative history, resulting in "light echoes" that encode the growth history of the SMBH. This implies that the map of the ionization state of the gas at different distances d from the SMBH reflects the ionizing luminosity output of the quasar at a time $t = d/c$. By observing sources located in the background of a foreground quasar, one can study the expected change in the

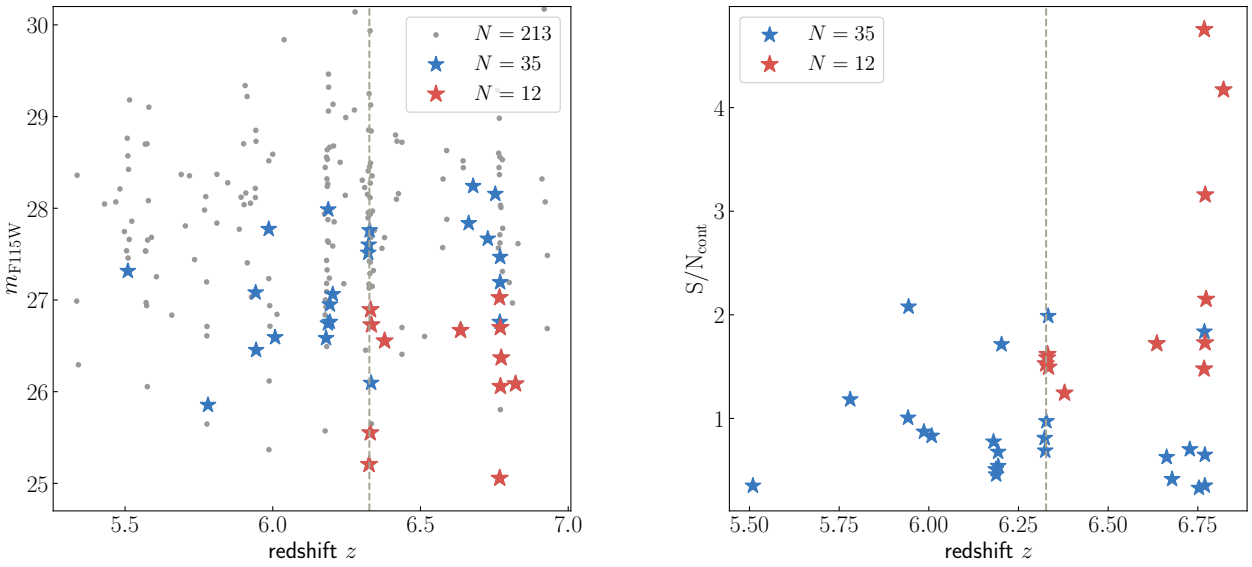

Figure 1. Sample of [O III]-emitting galaxies in the quasar field J0100+2802. A total of 213 [O III]-emitters (gray points) were previously discovered via NIRCam WFSS observations (D. Kashino et al. 2023) in this quasar field. For 35 of them (blue stars), we obtained deep NIRSpec/MSA spectroscopic observations, and 12 of those (red stars) were used in this analysis. Left and right panels show the observed magnitude in NIRCam's F115W filter and the galaxies' continuum signal-to-noise ratio per pixel as a function of redshift z, respectively.

Lyα forest opacity at close projected distances to the quasar to tomographically map the quasar's ionization field, which is a technique known as Lyα tomography (K.-G. Lee et al. 2014; T. M. Schmidt et al. 2019; K. Kakiichi et al. 2022).

Since galaxies in the background of luminous foreground quasars are often extremely faint, studies of the quasars' transverse proximity effect have so far focused on analyzing quasar pairs, where the environment of a foreground quasar is pierced by a single sightline to a background quasar at close distances projected in the plane of the sky. However, to date, only one spectroscopic detection of the transverse proximity effect has been reported using a pair of quasars at $z \sim 3$ in the He II Lyα forest observed in the spectrum of a background quasar at $z \approx 3$ (P. Jakobsen et al. 2003), while studies of several tens of other quasar pairs did not show the expected opacity change (T. M. Schmidt et al. 2018). However, in these studies, only a single sightline probes the environment of the foreground quasar, which makes it impossible to disentangle whether short quasar lifetimes or geometric obscuration effects that might prevent the sightline of the background object from being illuminated by the foreground quasar could be responsible for these nondetections.

At $z \gtrsim 6$ quasars are significantly less abundant than at lower redshifts (e.g., F. Wang et al. 2019; J.-T. Schindler et al. 2023), rendering studies of quasar pairs infeasible. The first detection of a photometric transverse proximity effect along a foreground quasar pierced by a background galaxy sightline was reported by S. E. I. Bosman et al. (2020) a few years ago, where a narrowband filter centered around the quasar's redshift at $z_{\rm QSO} \approx 5.8$ reveals a putative flux detection along the background sightline.

Here, we use a sample of 12 galaxies in the background of a luminous quasar in the high-redshift Universe to probe the transverse proximity effect for the first time spectroscopically and along multiple sightlines, and create the first three-dimensional map of a quasar's "light echo" by means of Lyα tomography. We leverage deep spectroscopic observations with the NIRSpec instrument on the James Webb Space Telescope (JWST) of a large number of faint galaxies that were detected behind a luminous quasar along our line of sight.

This Letter is organized as follows: In Section 2, we describe the observations of the galaxy spectra, while Section 3 shows the detection of the transverse proximity effect along multiple galaxy sightlines. We set up a model to describe the geometry of the quasar's ionized region and present the first map of the ionized region around the quasar using Lyα tomography in Section 4. In Section 5, we discuss the implications of our results on the growth of SMBHs in the early Universe.

2. Spectroscopic Observations of Galaxies Located behind a Luminous Quasar

2.1. Observations and Data Reduction

Previously, deep observations with JWST in NIRCam wide-field slitless (WFSS) mode obtained by the EIGER collaboration (D. Kashino et al. 2023) revealed a spectacular overdensity of bright, star-forming galaxies in the background of the superluminous, high-redshift quasar, J0100+2802 at $z_{\rm QSO} = 6.3270$ hosting a $\sim 10^{10}\,M_{\odot}$ SMBHs at its core (X.-B. Wu et al. 2015; A.-C. Eilers et al. 2023; M. Yue et al. 2024). We obtained follow-up spectroscopic observations using Multi-Object Spectroscopy with the NIRSpec instrument on JWST as part of the "Mapping a Super-luminous Quasar's Extended Radiative Emission" (MASQUERADE) program (program ID: #4713). Two masks were designed in this quasar field to obtain spectra with the F070LP filter and G140M grating for a subset of 35 of the, in total, 213 detected [O III]-emitters in the quasar field at $5.3 \lesssim z_{\rm gal} \lesssim 6.9$, shown in Figure 1. For the mask design, we prioritized bright (F115W $\lesssim$ 27 mag) galaxies that lie in the background or environment of the quasar, i.e., at $z_{\rm gal} \gtrsim z_{\rm QSO}$. The G140M/F070LP grating/filter combination covers the wavelength range of $0.70\,\mu{\rm m} < \lambda_{\rm obs} < 1.27\,\mu{\rm m}$, including the Ly$\alpha$ emission at the systemic redshift of the foreground quasar at $\lambda_{\rm obs} \approx 8907$ Å, with a nominal resolving power of $R \sim 1000$. The observations

were taken in 2024 December with a three-slitlet dither pattern in a 7.7 hr exposure for each mask. Six of these [O III]-emitters were covered by both masks and thus observed for a total of 15.4 hr.

The NIRSpec/Micro-Shutter Assembly (MSA) data are reduced using the `msaexp` (G. Brammer 2023) pipeline version 3, the details of which are described in A. de Graaff et al. (2025) and K. E. Heintz et al. (2025). In short, the pipeline first requires bias removal and cleaning of the MSA images from "snowballs," groups of pixels contaminated by cosmic rays. Next, it runs parts of the Level 2 JWST calibration pipeline, including identification of slits, extraction, flatfielding, and photometric calibration. Before combining, each exposure is corrected for wavelength-dependent bar-shadowing using a default 0.35 minimum value for inverse bar-shadow correction. The background subtraction is done directly on the two-dimensional slit cutouts and estimated in the area outside a box of 9 pixels centered on the line trace of the source. Finally, we perform an aperture extraction of 13 cross-dispersion pixels in the image cutouts to obtain the one-dimensional spectrum from combined and rectified exposures.

2.2. Flux Continuum Normalization

The observed galaxies have low metallicities (J. Matthee et al. 2023) and thus we fit a power law, i.e., $f_\lambda \propto (\lambda_{\rm rest}/1500\ \text{Å})^\beta$, to the unabsorbed wavelengths between $1300 < \lambda_{\rm rest} < 1700$ Å to estimate the galaxies' unabsorbed continuum flux. We extrapolate the power law to the bluer wavelength region, in order to continuum normalize the flux in the galaxies' Lyα forest and estimate the level of flux transmission. At wavelengths close to the galaxies' systemic redshifts, any transmitted flux might arise from ionized gas in the IGM or within the galaxies' circumgalactic medium (CGM), while at larger distances any flux transmission arises from highly ionized intergalactic gas. Thus, for galaxies with a redshift close to the systemic redshift of the quasar, we mask conservatively all spectral regions within $\Delta v \leqslant 1000\,{\rm km\,s^{-1}}$ of the galaxies' Lyα emission line, in order to avoid contamination of the flux transmission signal due to ionized gas in the CGM of the galaxies themselves.

In order to calibrate the flux in the galaxy spectra and account for any potential wavelength dependencies of the NIRSpec data, we compare the NIRSpec/MSA spectrum of the central quasar, J0100+2802, with a well-calibrated ground-based quasar spectrum observed with the Folded Port Infrared Echellette (R. A. Simcoe et al. 2008) spectrograph on the Magellan Telescopes and the X-Shooter spectrograph (J. Vernet et al. 2011) on the Very Large Telescope. The observations and data reduction of the ground-based quasar spectrum were previously presented (A.-C. Eilers et al. 2023). We rescale the NIRSpec/MSA spectrum to match the slope of the ground-based quasar spectrum at wavelengths longer than the Lyα emission line and fit a power law to the ratio of both spectra, which we then use to rescale all galaxy spectra. The correction factor is small, i.e., $\times$1–1.5, and varies smoothly across the relevant wavelength range, thus resulting in only minor corrections of the galaxy spectra.

We estimate the signal-to-noise ratio of the galaxies' unabsorbed continuum emission $\rm SN_{cont}$ per pixel between $1300 < \lambda_{\rm rest} < 1700$ Å, i.e., at wavelengths redwards of their Lyα emission line. The detection of the galaxies' continuum emission is essential, in order to search for the expected transmitted Lyα flux in the galaxy spectra due to a change in IGM opacity. For 14 galaxies at $z_{\rm gal} \gtrsim z_{\rm QSO}$, we were able to detect the continuum emission with $\rm SN_{cont} \geqslant 1$ per 6 Å pixel, which corresponds to approximately 150–180 $\rm km\,s^{-1}$ over the considered wavelength range. However, for two galaxies, the Lyα emission at the quasar's systemic redshift falls into the chip gap of the NIRSpec detectors, which can therefore not be used for our analysis.

The resulting 12 objects that meet our selection criteria for this analysis are shown in Figures 2 and 3, and their properties are listed in Table 1.

3. Detection of the Transverse Proximity Effect

We search for transmitted flux from the galaxies' UV continuum emission in their spectra bluewards of their Lyα emission line at wavelengths close to the systemic redshift of the foreground quasar, i.e., at $\lambda_{\rm obs} \approx 8907$ Å. We exclude the spectral range close to the galaxies' systemic redshift to avoid any contamination from the galaxies' Lyα emission line. At the quasar's redshift, the Universe is only $\sim$870 Myr old ($\sim$6% of its current age) and thus mostly opaque to Lyα photons (A.-C. Eilers et al. 2018; J. Yang et al. 2020; S. E. I. Bosman et al. 2022), which implies that any significant detection of Lyα forest transmission of the galaxies' UV continuum requires the quasar's proximity effect.

Our observations reveal the quasar's "light echo," and show the expected flux transmission in the Lyα forest due to the transverse proximity effect. For the first time we can observe the effect both along individual galaxy sightlines (two examples shown in Figure 2), as well as in the unweighted stacked transmission spectrum from all 12 galaxy sightlines shown in Figure 4, which indicates that the quasar's radiation not only ionized the IGM along our line of sight but also in the transverse direction, carving out large bubbles of highly ionized gas in its environment. The flux transmission spectra along all individual galaxy sightlines at the redshift of the foreground quasar are shown in Figure 5.

4. Modeling the Extent and Geometry of the Ionization Cone

The detection of the transverse proximity effect along multiple galaxy sightlines enables us to model the extent and geometry of the quasar's ionization cone. Inspired by the unification model of active galactic nuclei (e.g., R. Antonucci 1993; C. M. Urry & P. Padovani 1995), we construct a model with a biconical ionization geometry to create a three-dimensional map of the quasar's light echo, and to determine the onset of the quasar's UV-luminous lifetime.

Luminous quasars ionize their surroundings with an ionizing emissivity $\Gamma_{\rm QSO}$, which depends on the quasars' ionizing photon emission rate $\dot{N}_{\rm ion}$. The total number of ionizing photons emitted by a quasar can then be written as $N_{\rm ion} = \int \dot{N}_{\rm ion} dt$ (F. B. Davies et al. 2019). We assume a luminosity-dependent bolometric correction (J. C. Runnoe et al. 2012) to convert the quasars' absolute magnitude at 1450 Å in the rest frame, i.e., $M_{1450} = -29.26$ (X.-B. Wu et al. 2015), to an ionizing luminosity assuming a spectral energy distribution (E. Lusso et al. 2015). This results in a bolometric luminosity of $L_{\rm bol} \approx 9.7 \times 10^{47} {\rm erg\,s^{-1}}$, which corresponds to a rate of ionizing photons of $\dot{N}_{\rm ion} \approx 1.1 \times 10^{58}\,{\rm s^{-1}}$ for the central quasar, J0100+2802. The ionizing emissivity $\Gamma_{\rm QSO}$ is linearly

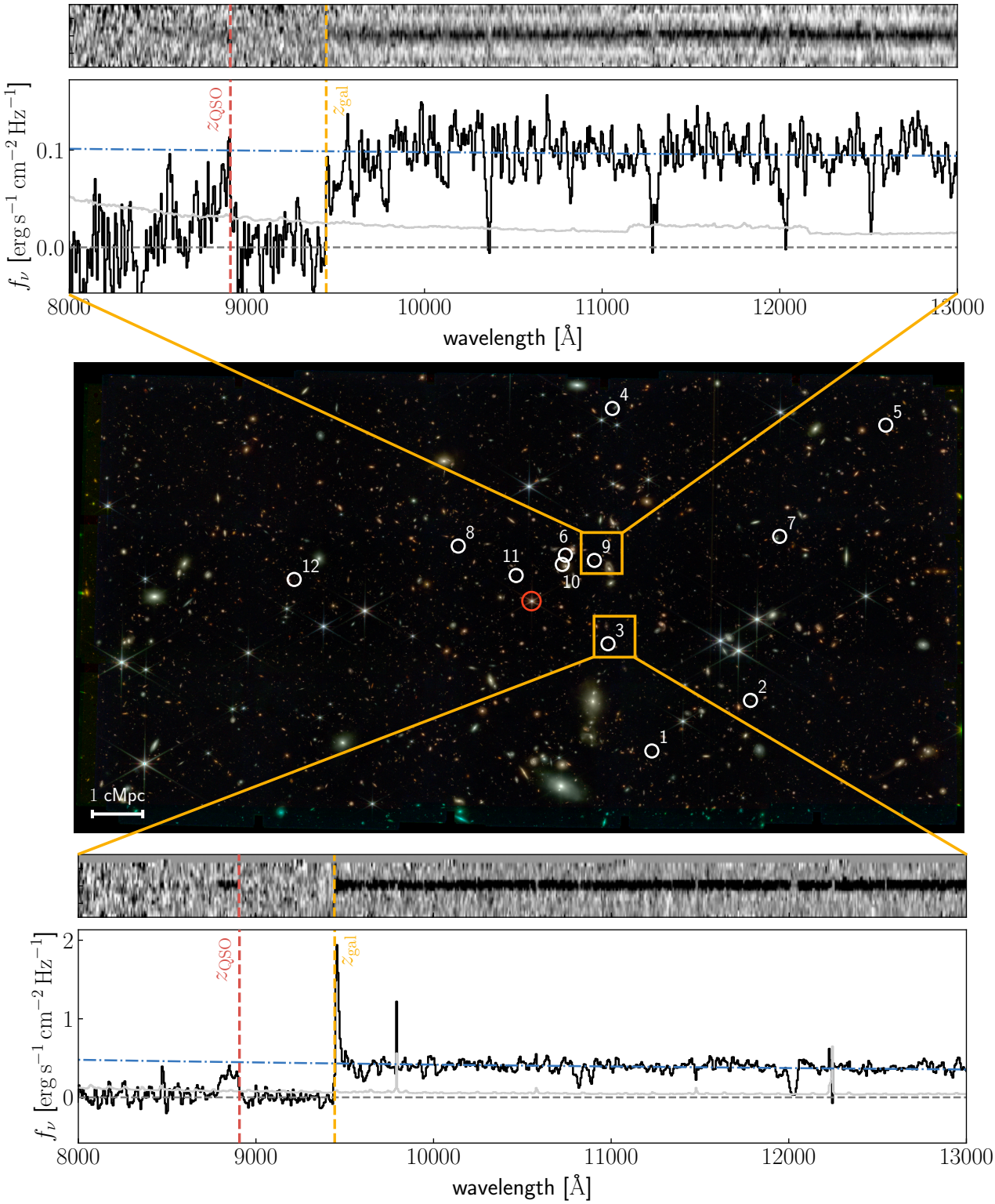

Figure 2. Observations. The middle panel shows a color image of the quasar field with the central quasar circled in red, constructed via NIRCam images in the filters F115W, F200W, and F356W, showing the spatial locations of the 12 analyzed background galaxies, circled in white. The top and bottom panels show the two-dimensional and one-dimensional spectra of two galaxies, which show a clear detection of the transverse proximity effect at the systemic redshift of the quasar $z_{\rm QSO}$ indicated by the red dashed line. The yellow dashed line shows the galaxies' redshift as determined from the [O III]-emission line, $z_{\rm gal}$, while the blue dashed–dotted line demonstrates the power-law fit to the unabsorbed galaxy continuum at $\lambda_{\rm rest} > \lambda_{\rm Ly\alpha}$, which is used to calculate the flux transmission and the optical depth within the Lyα forest.

proportional to $\dot{N}_{\rm ion}$, i.e., $\Gamma_{\rm QSO} = \frac{-\beta\ \sigma_{912}\ \dot{N}_{\rm ion}}{(3-\beta)\ 4\pi\ (d_\parallel^2 + d_\perp^2)}$, where $d_\parallel$ and $d_\perp$ describe the distance along the line of sight and perpendicular to the quasar, respectively, while $\beta = -1.5$ and $\sigma_{912} = 6.3 \times 10^{-18}\,{\rm cm}^2$ denotes the power-law slope of the quasar's ionizing spectrum and the absorption cross section of neutral hydrogen to ionizing photons.

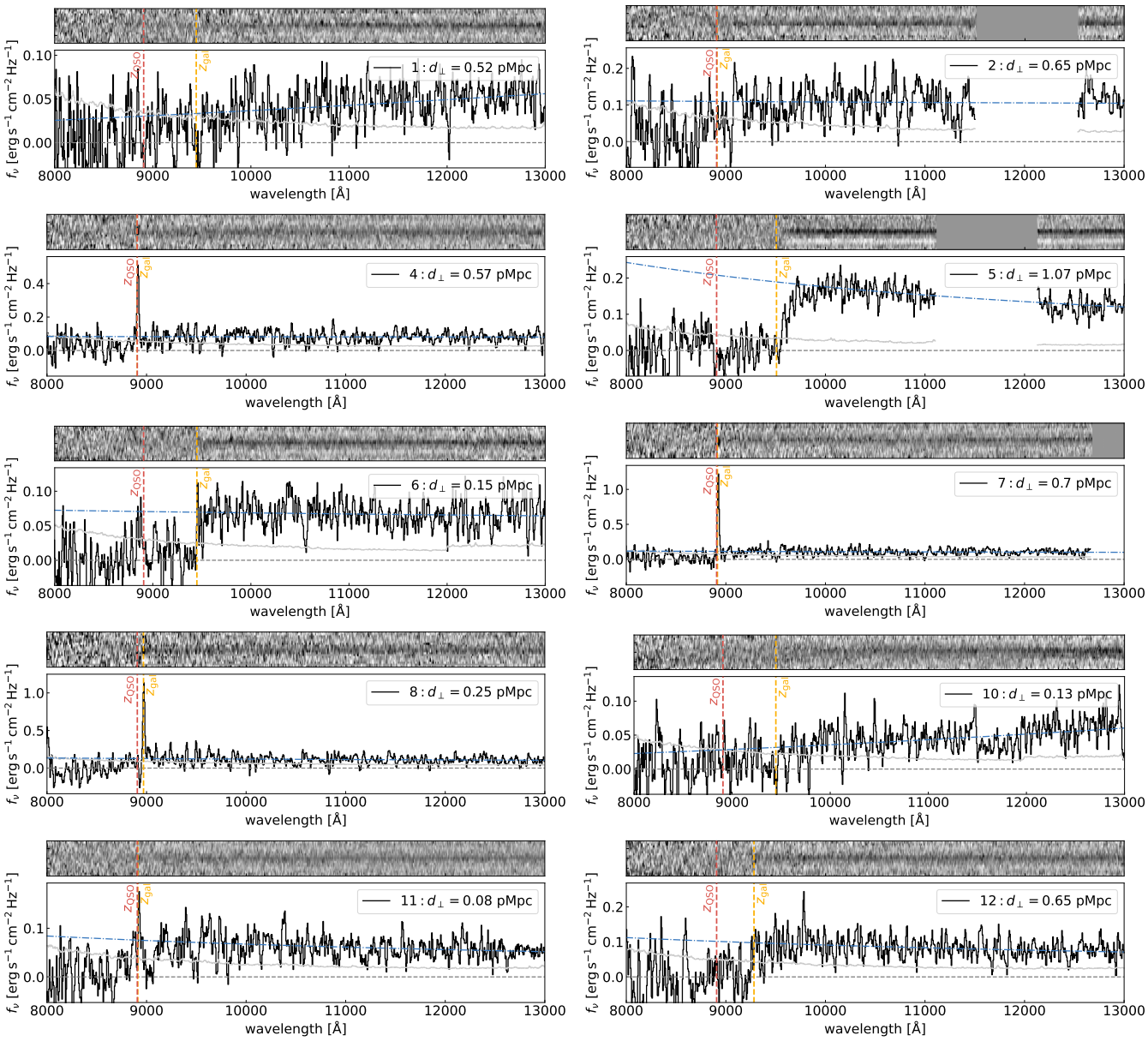

Figure 3. Galaxy spectra. Two-dimensional (top) and one-dimensional (bottom) spectra of 10 out of the 12 analyzed galaxies in the quasar field (the remaining two galaxy spectra are shown in Figure 2). The red and yellow dashed lines indicate the systemic redshift of the quasar z_{QSO} as well as the galaxy's redshift z_{gal}, respectively. Blue dashed–dotted lines show the power-law fit to the unabsorbed galaxy continuum emission.

The total photoionization rate $\Gamma_{\rm H\,I}$ at each spatial location in the observed volume is determined via a superposition of $\Gamma_{\rm QSO}$ and the ionizing emissivity of the UV background $\Gamma_{\rm UVB}$, which is estimated to be $\Gamma_{\rm UVB} \approx 3 \times 10^{-13}{\rm s}^{-1}$ based on recent optical depth measurements along quasar sightlines (S. E. I. Bosman et al. 2022), which we extrapolate to the redshift of the quasar $z_{\rm QSO}$. These measurements correspond to a mean transmitted flux measurement of $\langle F \rangle \approx 0.0043$ (S. E. I. Bosman et al. 2022). We neglect any small intrinsic scatter due to density fluctuations and calculate the effective optical depth of the Lyα forest as $\tau^{\alpha}_{\rm eff} \approx \gamma \times (\Gamma_{\rm H\,I}/2.5 \times 10^{13}{\rm s}^{-1})^{-\delta}$, where the parameters $\gamma \approx 6$ and $\delta \approx 0.55$ were derived from a fit to an ensemble of simulated Lyα forest spectra from hydrodynamical simulations (F. B. Davies et al. 2020a).

Because the quasar resides in an environment with an observed galaxy overdensity (D. Kashino et al. 2023; A.-C. Eilers et al. 2024), we briefly assess the galaxies' influence on the ionizing photon budget. Using the canonical value for the ionizing production efficiency, $\log_{10}\xi_{\rm ion} = 25.2$ (J. Matthee et al. 2017; C. Simmonds et al. 2024), and assuming an ionizing escape fraction of $f_{\rm esc} \approx 3\%$ (S. Mascia et al. 2024; C. Papovich et al. 2025; M. Yue et al. 2025), we sum the UV luminosity of all galaxies within the quasar environment, i.e., $|z_{\rm gal} - z_{\rm QSO}| < 0.05$, and find a photon production rate of $\dot{N}_{\rm ion,gal} = 6.8 \times 10^{-58}{\rm s}^{-1}$, which is more than 5 orders of magnitude lower than the ionizing photons emitted by the quasar. We thus neglect any effects due to the galaxies in the quasar's environment.

Our model for the quasar's ionized region describes the geometry of the ionization cone with three parameters: an inclination i, an orientation described by a position angle PA, as well as an opening angle ψ of the obscuring medium, which corresponds to an obscured solid angle fraction as $f_{\rm obsc} = 1 - [2\sin^2((90^\circ - \psi)/2)]$. The effect of each model parameter on the geometry of the ionization cone and the

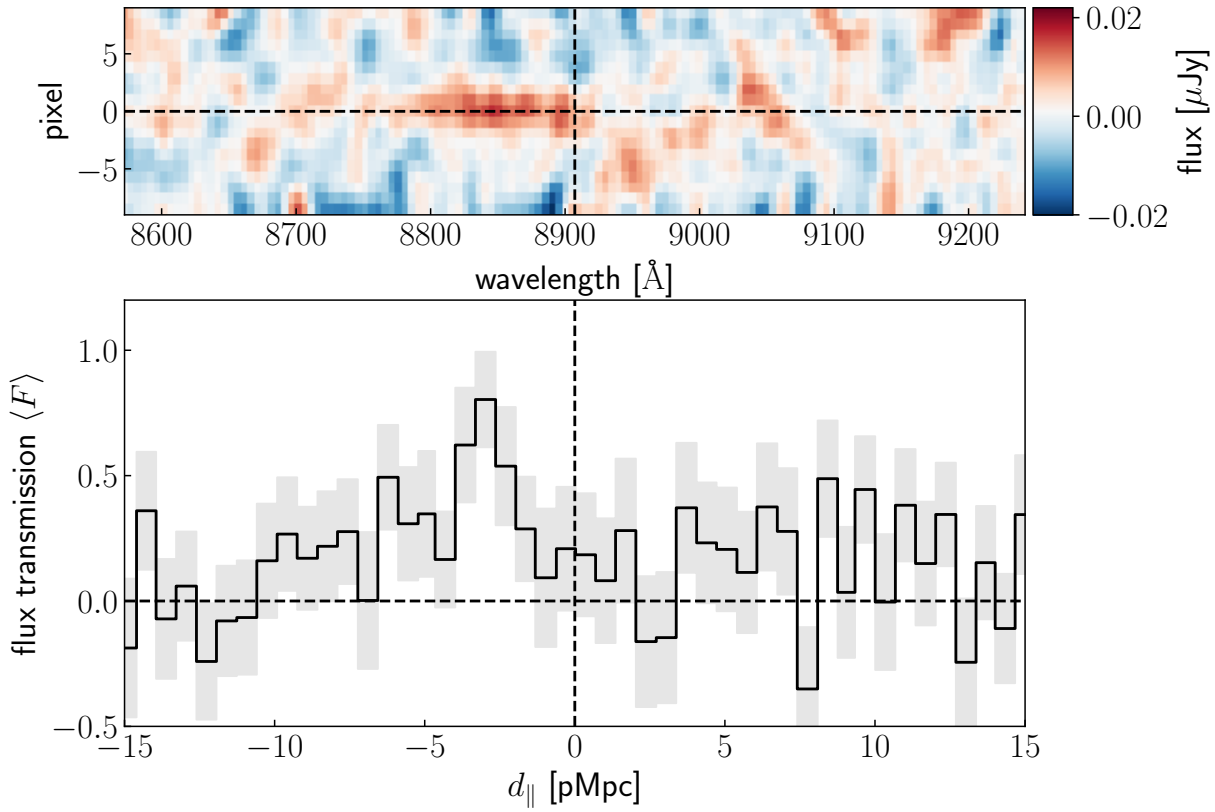

Figure 4. Stacked galaxy spectra. The top panel shows the two-dimensional unweighted mean stack of all 12 galaxy spectra colored by the flux. The bottom panel shows the unweighted stack over the same wavelength range of the continuum normalized one-dimensional galaxy spectra binned to 500 km s^{-1} pixels around the quasar's systemic redshift, which is indicated by the vertical black dashed lines at $d_\parallel = 0$ pMpc or $\lambda_{\mathrm{Ly}\alpha} \approx 8907$ Å. The horizontal dashed line indicates the spectral trace in the top panel, while it denotes the zero flux level in the bottom panel. Note that the two-dimensional spectra are not normalized by the galaxies' continuum emission before stacking, while we did normalize the one-dimensional spectra to show the stacked Lyα transmitted flux.

Table 1
Observed Galaxies

Galaxy	ID	R.A. hh:mm:ss.sss	Decl. dd:mm:ss.sss	z_{gal}	F115W (mag)	$d_\perp$ (pMpc)	$\mathrm{S/N_{cont}}$	β
1	2084	01:00:19.932	+28:02:16.775	6.77	27.0	0.52	1.5	-0.38 ± 0.44
2	4222	01:00:20.351	+28:01:24.026	6.33	25.6	0.65	1.6	-2.12 ± 0.71
3	6733	01:00:15.822	+28:02:06.311	6.77	25.1	0.24	4.8	-2.61 ± 0.21
4	10998	01:00:08.792	+28:01:03.038	6.33	25.2	0.57	1.5	-2.08 ± 0.44
5	11981	01:00:14.698	+27:59:17.849	6.82	26.1	1.07	4.2	-3.45 ± 0.18
6	12217	01:00:12.299	+28:02:00.209	6.77	26.4	0.15	2.2	-2.24 ± 0.29
7	16479	01:00:15.967	+28:00:29.464	6.33	26.7	0.70	1.5	-2.33 ± 0.45
8	16759	01:00:09.908	+28:02:40.789	6.38	26.6	0.25	1.2	-2.52 ± 0.54
9	17385	01:00:13.032	+28:01:49.991	6.77	26.1	0.20	3.2	-2.15 ± 0.22
10	17577	01:00:12.520	+28:02:03.904	6.77	26.7	0.13	1.7	0.0 ± 0.40
11	18061	01:00:11.942	+28:02:25.277	6.33	26.9	0.08	1.6	-3.00 ± 0.38
12	18268	01:00:07.674	+28:03:55.250	6.64	26.7	0.65	1.7	-2.94 ± 0.36

Note. Columns show the galaxy number and ID, coordinates R.A. and decl., the galaxy's redshift as determined from its [O III] emission lines, the observed magnitude in the NIRCam/F115W filter, its transverse distance from the central quasar, as well as the continuum signal-to-noise ratio (S/N) per pixel and the slope of the power-law fit to its continuum emission.

resulting expected transmitted flux is shown in Figure 6. Additionally, we model the UV-luminous lifetime of the quasar t_{QSO} assuming a constant quasar luminosity, i.e., a "light-bulb" light curve. The onset of the quasar's UV-luminous radiation started at a time t_{QSO} ago, launching an ionization front that is propagating outwards with the speed of light c. The finite emission timescale results in a parabolic cut-off of the quasar's radiation seen from our point of view, as illustrated in the right panel of Figure 6.

The spatial regions within the emission cone are ionized by $\Gamma_{\mathrm{H\,I}} = \Gamma_{\mathrm{QSO}} + \Gamma_{\mathrm{UVB}}$, while the regions outside of the cones are ionized only by Γ_{UVB}. Thus, any galaxy sightline piercing through the ionization cone is expected to show Lyα transmitted flux around the systemic redshift of the quasar, as the residual neutral hydrogen in the IGM is ionized by the intense light from the quasar, reducing the opacity to Lyα photons. The regions outside of the illuminated cone are influenced only by the UV background radiation and are thus set to the mean flux

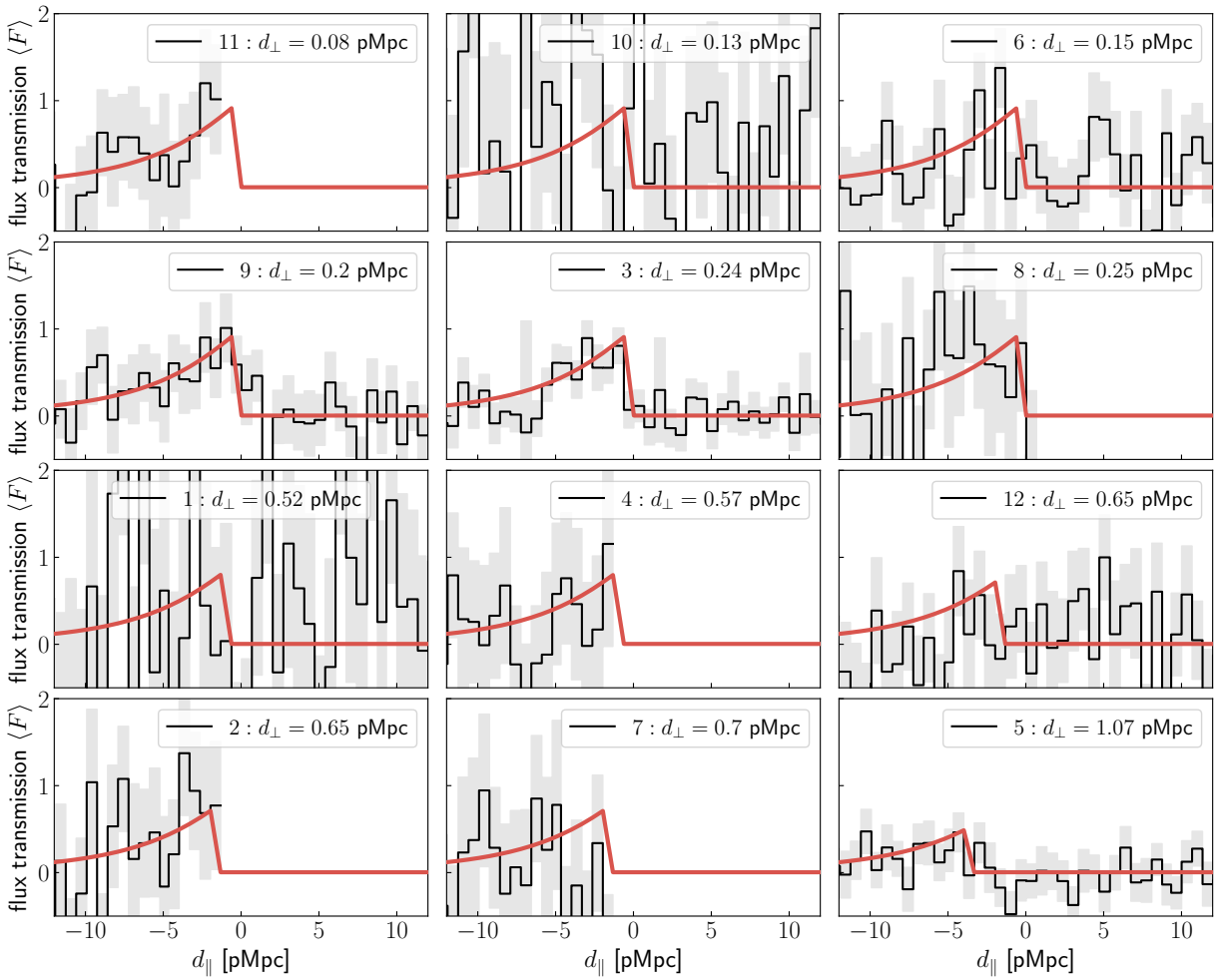

Figure 5. Flux transmission along individual galaxy sightlines. The panels show the continuum-normalized, transmitted flux (black) around the systemic redshift of the quasar at $d_\parallel = 0$ pMpc with spectral uncertainties (gray) along the 12 background galaxy sightlines, which are used to model the quasar's ionization cone. The red lines show the expected transmission profile from the best fit of the quasar's ionization cone extracted at each galaxy's location on the sky (see Section 4).

transmission of $\langle F \rangle \approx 0.0043$ at this redshift (S. E. I. Bosman et al. 2022).

Each of the observed galaxies in the background of the quasar pierce through the emission cone at the sky location ($x_{\rm gal}$, $y_{\rm gal}$) (with the central quasar located at (0,0)), at a distance from the quasar projected into the plane of the sky of $d_\perp = \sqrt{x_{\rm gal}^2 + y_{\rm gal}^2}$, while each spectral pixel along the galaxy sightline has a parallel distance to the quasar of $d_\parallel = \Delta v / H(z_{\rm QSO})$, where Δv describes the velocity shift with respect to the systemic redshift of the quasar, and $H(z_{\rm QSO})$ denotes the Hubble constant at the quasar's redshift. We calculate the intersections between the surface of the double cone for each galaxy sightline following a model developed for the analysis of protoplanetary disks (K. A. Rosenfeld et al. 2013).

For a given set of parameters for the ionization cone, we model the expected flux profile for each galaxy given its position on the sky ($x_{\rm gal}$, $y_{\rm gal}$) with respect to the quasar and compare the predicted flux transmission to the observed continuum-normalized galaxy spectra. All model parameters are determined via a Markov Chain Monte Carlo (MCMC) algorithm (D. Foreman-Mackey et al. 2013) with a likelihood function $\ln \mathcal{L} = \sum_i - \frac{(f_i - f_{{\rm model},i})^2}{2\sigma_i^2}$, where f_i and σ_i denote the continuum-normalized flux and noise vectors of each galaxy i around the quasar's systemic redshift, i.e., between $8500 < \lambda_{\rm obs} < 9500$ Å (see Figure 5). The parameter $f_{{\rm model},i}$ describes the expected flux transmission extracted at each galaxy position on the sky given the four model parameters, i.e., i, PA, ψ, and $t_{\rm QSO}$. We choose flat priors for the four parameters, i.e., $i \in [0°, 90°)$, PA $\in [0°, 360°)$, $\log_{10}(1 - f_{\rm obsc}) \in [-4, 0]$, and $\log_{10}(t_{\rm QSO}/{\rm yr}) \in [4, 9]$. We apply an additional prior on the orientation of the ionization cone to ensure that our line of sight falls within the illuminated cone, since we would otherwise not expect to see a luminous, unobscured quasar. This latter assumption results in nonflat prior distributions for the inclination and the unobscured fraction, as shown in Figure 7.

Our best model for the quasar's ionization cone is depicted in Figure 8 and suggests a 1σ (2σ) upper limit on the opening angle of the obscuring medium of $\psi < 65°$ ($\psi < 71°$), corresponding to an obscured fraction of $f_{\rm obsc} < 91\%$ ($f_{\rm obsc} < 94\%$), and an onset of the UV-luminous quasar light $\log_{10}(t_{\rm QSO}/{\rm yr}) = 5.6^{+0.1}_{-0.3}$ ago. We also obtain weak constraints on the orientation and inclination of the ionization cone, indicating that a mildly inclined cone, i.e., $i \approx 15°$, with a position angle of $240° \lesssim {\rm PA} \lesssim 340°$ is preferred. Figure 7 shows the full posterior distributions of all model parameters.

Other factors, such as variability in the quasar's luminosity or precession of its bicone, may also affect the shape and

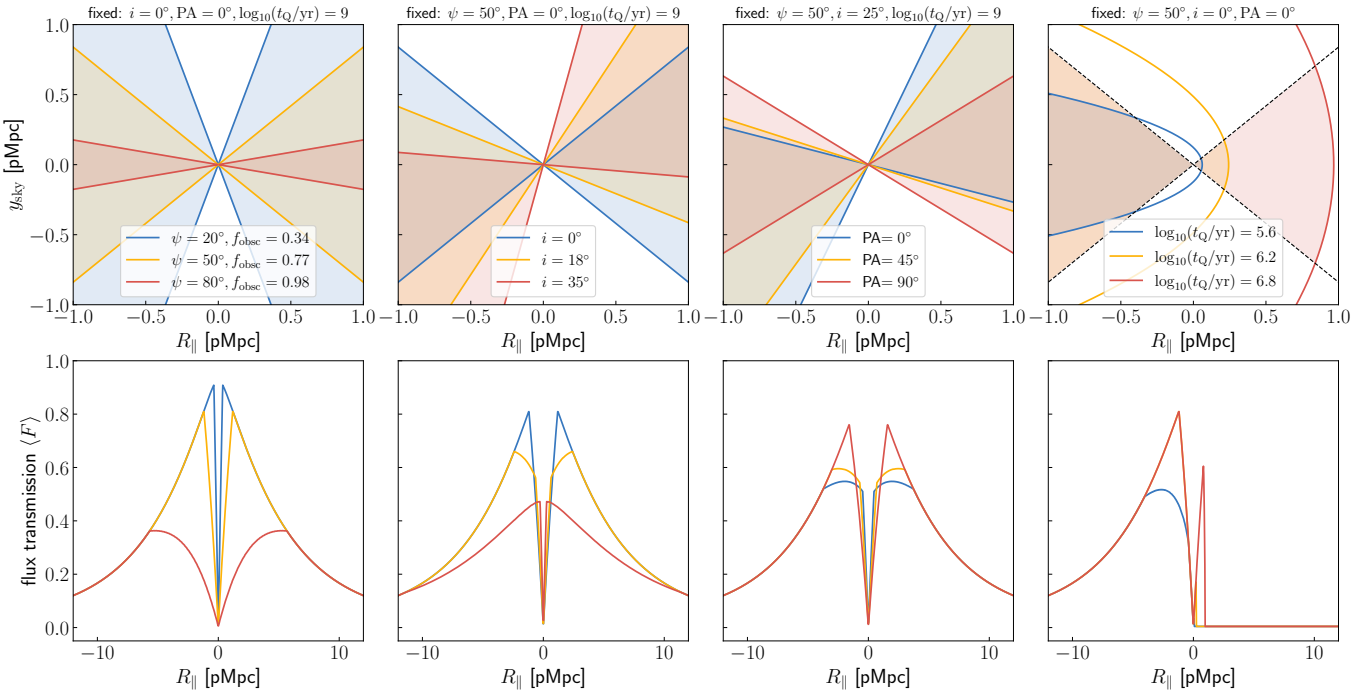

Figure 6. Biconical model for a quasar's ionization cone. Left to right: panels show the model for the ionization cone with varying parameters, i.e., the opening angle of the obscuring medium ψ, which corresponds to the solid angle obscured fraction f_{obsc}, the inclination of the cone i, the position angle PA, and the timescale of the quasar's UV-luminous radiation t_{QSO}. All other parameters are kept fixed to the values as indicated above each panel. The top panels show the illuminated area around the central quasar, while the bottom panels illustrate the expected mean transmitted flux profile for a highly idealized sample of 1000 galaxies, which are all aligned and equally distributed along one axis of the sky, y_{sky}, while $x_{\mathrm{sky}} = 0$.

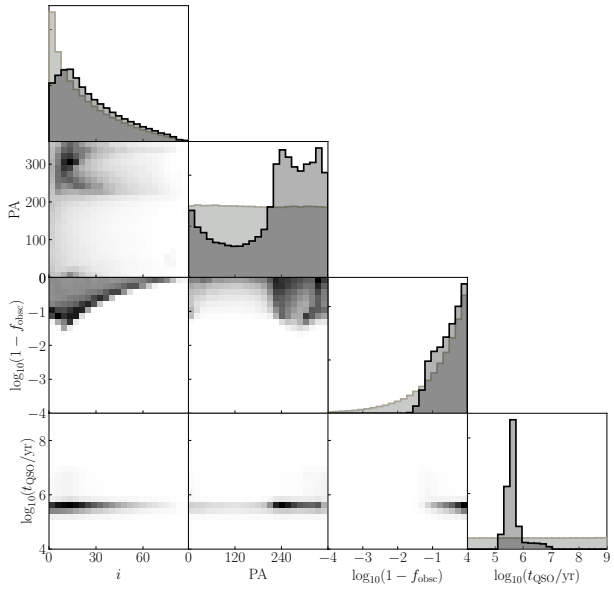

Figure 7. Posterior distributions of the model parameters for the ionization cone. Lower panels show the marginalized two-dimensional posterior probability distributions determined via MCMC of the four model parameters for the ionization cone, i.e., the inclination i, the position angle PA, the unobscured solid angle fraction $\log_{10}(1 - f_{\mathrm{obsc}})$, and the UV-luminous lifetime of the quasar $\log_{10}(t_{\mathrm{QSO}}/\mathrm{yr})$. Light and dark gray histograms in the top diagonal panels show the one-dimensional prior and posterior distributions, respectively.

extent of the surrounding ionized region. However, the limited number of bright background galaxies restricts our sensitivity to all solid angles, preventing us from constraining more complex, flexible models with additional free parameters.

5. Implications for the Early Growth of Black Holes

The estimate for the quasar lifetime t_{QSO} is significantly shorter than the time required to grow the quasar's approximately 10 billion solar mass black hole. Assuming Eddington-limited accretion with a canonical radiative efficiency of $\epsilon \approx 10\%$, we would expect the black hole accretion timescale to be comparable to the Hubble time at these redshifts, i.e., $\sim 10^{8-9}$ yr (e.g., K. Inayoshi et al. 2020). Our new estimate is, however, consistent with previous measurements of the quasar's lifetime, leveraging the extent of its observed proximity zone in the quasar's rest-UV spectrum along our sightline (A.-C. Eilers et al. 2017; F. B. Davies et al. 2020b). It also agrees well with the recent measurement of the average UV-luminous duty cycle of high-redshift quasars, i.e., $f_{\mathrm{duty}} \lesssim 1\%$ (A.-C. Eilers et al. 2024), inferred from the quasars' clustering strength measured by the cross-correlation of quasars with their surrounding galaxies, which represents a completely independent approach to estimate the quasars' activity timescales (A.-C. Eilers et al. 2024; E. Pizzati et al. 2024). Furthermore, the lack of significant flux transmission in the background of the quasar, as shown in Figure 4, suggests that there were no significant previous UV-luminous accretion episodes due to a potentially flickering quasar light curve (F. B. Davies et al. 2020a). If the quasar's radiation were episodic, the emission from previous active phases would continue to propagate outwards ionizing the gas along its path, thus resulting in lower opacity "shells" around the quasar (K. L. Adelberger 2004; S. E. I. Bosman et al. 2020).

Such short UV-luminous quasar lifetimes pose significant challenges to current black hole growth models, where matter from the surrounding accretion disk is accreted with a canonical radiative efficiency of $\epsilon \approx 10\%$. If a very high fraction of >99% of growing black holes in the early Universe

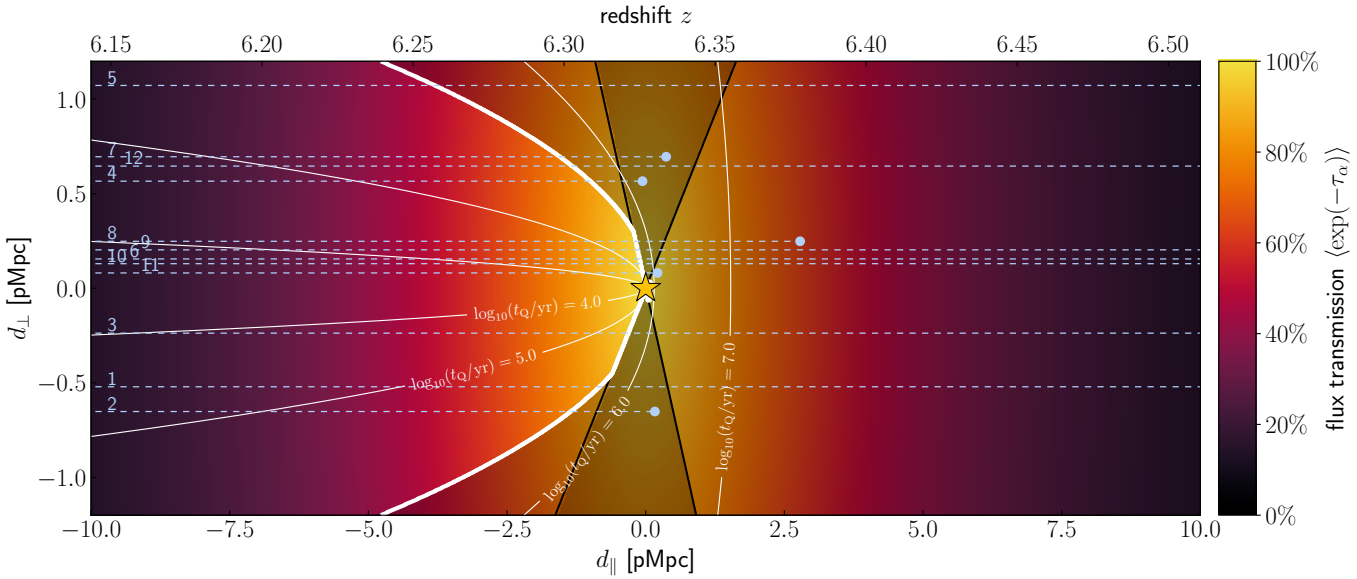

Figure 8. Map of the quasar's ionized bubble. The central quasar is indicated by the yellow star, and all galaxy sightlines are shown as blue dashed lines. The underlying colormap indicates the level of the expected Lyα flux transmission, while the overplotted black contours illustrate the best-fit ionization cone. The thin white parabolas show isochrones, i.e., outlines of the quasar's light echo at different times, while the thick white line indicates the best fit to our data of $\log_{10}(t_{\mathrm{QSO}}/\mathrm{yr}) = 5.7^{+0.1}_{-0.3}$. Thus, all shaded regions are not illuminated by the quasar, and only the congruence of the ionization cone and illuminated parabola due to the quasar's light echo is illuminated.

were obscured by dust or dense gas, one could reconcile the required long black hole growth timescales with the significantly shorter observed UV-luminous timescales (e.g., F. B. Davies et al. 2019; S. Satyavolu et al. 2023b), prompting many studies to search for the predicted abundance of highly obscured quasars. However, identifying obscured high-redshift quasars with SMBHs has been challenging due to the lack of sensitive wide-field mid-infrared or X-ray surveys, and thus only very few promising candidates have been discovered to date (R. Endsley et al. 2022; S. Fujimoto et al. 2022). Our detection of the transverse proximity effect of the quasar along multiple galaxy sightlines indicates that at least this high-redshift quasar is not highly obscured. We can securely rule out a solid angle obscured fraction of >99% at $>5\sigma$ significance, and our best estimate is in line with the fraction of obscured quasars at lower redshifts as determined from deep multiwavelength wide-field surveys (M. Polletta et al. 2008).

Thus, our results imply that sightline-dependent obscuration effects due to the geometry of an obscuring medium around the accreting black hole cannot exclusively account for the observed short UV-luminous black hole growth timescales of high-redshift quasars. In order to explain the existence of several billion solar mass black holes at early cosmic times, it is thus likely that these black holes accrete matter at radiatively inefficient accretion rates, i.e., $\epsilon \ll 10\%$, as suggested in slim accretion disk models for instance (e.g., R. Narayan & I. Yi 1995; R. D. Blandford & M. C. Begelman 1999; M. C. Begelman & M. Volonteri 2017). In addition, black holes could grow in initially completely enshrouded cocoons, before their radiation pressure sheds off any obscuring medium, manifesting themselves as UV-luminous quasars—a scenario that would imply the existence of a very large number of obscured quasars hosting SMBHs in the early Universe. One can speculate that the recently JWST-discovered galaxies dubbed "little red dots" host smaller black holes in an early, obscured growth phase (J. Matthee et al. 2024; R. P. Naidu et al. 2025), but a large population of obscured massive black holes is yet to be detected.

Acknowledgments

This work is based on observations made with the NASA/ESA/CSA James Webb Space Telescope. The data were obtained from the Mikulski Archive for Space Telescopes at the Space Telescope Science Institute, which is operated by the Association of Universities for Research in Astronomy, Inc., under NASA contract NAS 5-03127 for JWST. These observations are associated with programs #1243 and #4713.

All of the data presented in this Letter were obtained from the Mikulski Archive for Space Telescopes (MAST) at the Space Telescope Science Institute. The specific observations analyzed can be accessed via doi:10.17909/w7hm-qb39.

J.M. is supported by the European Union (ERC, AGENTS, 101076224).

Software: numpy (C. R. Harris et al. 2020), scipy (E. Jones et al. 2001), matplotlib (J. D. Hunter 2007), astropy (Astropy Collaboration et al. 2013, 2018, 2022), emcee (D. Foreman-Mackey et al. 2013).

ORCID iDs

Anna-Christina Eilers https://orcid.org/0000-0003-2895-6218
Minghao Yue https://orcid.org/0000-0002-5367-8021
Jorryt Matthee https://orcid.org/0000-0003-2871-127X
Joseph F. Hennawi https://orcid.org/0000-0002-7054-4332
Frederick B. Davies https://orcid.org/0000-0003-0821-3644
Robert A. Simcoe https://orcid.org/0000-0003-3769-9559
Richard Teague https://orcid.org/0000-0003-1534-5186
Rongmon Bordoloi https://orcid.org/0000-0002-3120-7173
Gabriel Brammer https://orcid.org/0000-0003-2680-005X
Daichi Kashino https://orcid.org/0000-0001-9044-1747

Ruari Mackenzie https://orcid.org/0000-0003-0417-385X
Rohan P. Naidu https://orcid.org/0000-0003-3997-5705
Benjamín Navarrete https://orcid.org/0000-0002-6417-040X

References

Adelberger, K. L. 2004, ApJ, 612, 706
Antonucci, R. 1993, ARA&A, 31, 473
Astropy Collaboration, Price-Whelan, A. M., Lim, P. L., et al. 2022, ApJ, 935, 167
Astropy Collaboration, Price-Whelan, A. M., Sipőcz, B. M., et al. 2018, AJ, 156, 123
Astropy Collaboration, Robitaille, T. P., Tollerud, E. J., et al. 2013, A&A, 558, A33
Begelman, M. C., & Volonteri, M. 2017, MNRAS, 464, 1102
Begelman, M. C., Volonteri, M., & Rees, M. J. 2006, MNRAS, 370, 289
Blandford, R. D., & Begelman, M. C. 1999, MNRAS, 303, L1
Bosman, S. E. I., Kakiichi, K., Meyer, R. A., et al. 2020, ApJ, 896, 49
Bosman, S. E. I., Davies, F. B., Becker, G. D., et al. 2022, 514, 55
Brammer, G. 2023, msaexp: NIRSpec analyis tools, v0.6.17, Zenodo, doi:10.5281/zenodo.8319596
Carilli, C. L., Wang, R., Fan, X., et al. 2010, ApJ, 714, 834
Davies, F. B., Hennawi, J. F., & Eilers, A.-C. 2019, ApJL, 884, L19
Davies, F. B., Hennawi, J. F., & Eilers, A.-C. 2020a, MNRAS, 493, 1330
Davies, F. B., Wang, F., Eilers, A.-C., & Hennawi, J. F. 2020b, ApJL, 904, L32
de Graaff, A., Brammer, G., Weibel, A., et al. 2025, A&A, 697, A189
Eilers, A.-C., Davies, F. B., & Hennawi, J. F. 2018, ApJ, 864, 53
Eilers, A.-C., Davies, F. B., Hennawi, J. F., et al. 2017, ApJ, 840, 24
Eilers, A.-C., Hennawi, J. F., Decarli, R., et al. 2020, ApJ, 900, 37
Eilers, A.-C., Mackenzie, R., Pizzati, E., et al. 2024, ApJ, 974, 275
Eilers, A.-C., Simcoe, R. A., Yue, M., et al. 2023, ApJ, 950, 68
Endsley, R., Stark, D. P., Fan, X., et al. 2022, MNRAS, 512, 4248
Fan, X., Strauss, M. A., Becker, R. H., et al. 2006, AJ, 132, 117
Foreman-Mackey, D., Hogg, D. W., Lang, D., & Goodman, J. 2013, PASP, 125, 306
Fujimoto, S., Brammer, G. B., Watson, D., et al. 2022, Natur, 604, 261
Harris, C. R., Millman, K. J., van der Walt, S. J., et al. 2020, Natur, 585, 357
Heintz, K. E., Brammer, G. B., Watson, D., et al. 2025, A&A, 693, A60
Hunter, J. D. 2007, CSE, 9, 90
Inayoshi, K., Haiman, Z., & Ostriker, J. P. 2016, MNRAS, 459, 3738
Inayoshi, K., Visbal, E., Haiman, Z., et al. 2020, ARA&A, 58, 27
Jakobsen, P., Jansen, R. A., Wagner, S., & Reimers, D. 2003, A&A, 397, 891
Jones, E., Oliphant, T., Peterson, P., et al. 2001, SciPy: Open Source Scientific Tools for Python, http://www.scipy.org/
Kakiichi, K., Schmidt, T., & Hennawi, J. 2022, MNRAS, 516, 582
Kashino, D., Lilly, S. J., Matthee, J., et al. 2023, ApJ, 950, 66
Lee, K.-G., Hennawi, J. F., Stark, C., et al. 2014, ApJL, 795, L12
Lusso, E., Worseck, G., Hennawi, J. F., et al. 2015, MNRAS, 449, 4204
Mascia, S., Pentericci, L., Calabrò, A., et al. 2024, A&A, 685, A3
Matthee, J., Mackenzie, R., Simcoe, R. A., et al. 2023, ApJ, 950, 67
Matthee, J., Naidu, R. P., Brammer, G., et al. 2024, ApJ, 963, 129
Matthee, J., Sobral, D., Best, P., et al. 2017, MNRAS, 465, 3637
Morey, K. A., Eilers, A.-C., Davies, F. B., Hennawi, J. F., & Simcoe, R. A. 2021, ApJ, 921, 88
Naidu, R. P., Matthee, J., Katz, H., et al. 2025, arXiv:2503.16596
Narayan, R., & Yi, I. 1995, ApJ, 452, 710
Papovich, C., Cole, J. W., Hu, W., et al. 2025, arXiv:2505.08870
Pizzati, E., Hennawi, J. F., Schaye, J., et al. 2024, MNRAS, 534, 3155
Polletta, M., Weedman, D., Hönig, S., et al. 2008, ApJ, 675, 960
Rosenfeld, K. A., Andrews, S. M., Hughes, A. M., Wilner, D. J., & Qi, C. 2013, ApJ, 774, 16
Runnoe, J. C., Brotherton, M. S., & Shang, Z. 2012, MNRAS, 422, 478
Satyavolu, S., Eilers, A.-C., Kulkarni, G., et al. 2023a, MNRAS, 522, 4918
Satyavolu, S., Kulkarni, G., Keating, L. C., & Haehnelt, M. G. 2023b, MNRAS, 521, 3108
Schindler, J.-T., Bañados, E., Connor, T., et al. 2023, ApJ, 943, 67
Schmidt, T. M., Hennawi, J. F., Lee, K.-G., et al. 2019, ApJ, 882, 165
Schmidt, T. M., Hennawi, J. F., Worseck, G., et al. 2018, ApJ, 861, 122
Shakura, N. I., & Sunyaev, R. A. 1973, A&A, 500, 33
Simcoe, R. A., Burgasser, A. J., Bernstein, R. A., et al. 2008, Proc. SPIE, 7014, 70140U
Simmonds, C., Tacchella, S., Hainline, K., et al. 2024, MNRAS, 535, 2998
Soltan, A. 1982, MNRAS, 200, 115
Tanaka, T., & Haiman, Z. 2009, ApJ, 696, 1798
Urry, C. M., & Padovani, P. 1995, PASP, 107, 803
Vernet, J., Dekker, H., D'Odorico, S., et al. 2011, A&A, 536, A105
Visbal, E., & Croft, R. A. C. 2008, ApJ, 674, 660
Wang, F., Yang, J., Fan, X., et al. 2019, ApJ, 884, 30
Wu, X.-B., Wang, F., Fan, X., et al. 2015, Natur, 518, 512
Yang, J., Wang, F., Fan, X., et al. 2020, ApJ, 904, 26
Yu, Q., & Tremaine, S. 2002, MNRAS, 335, 965
Yue, M., Eilers, A.-C., Matthee, J., et al. 2025, arXiv:2507.05381
Yue, M., Eilers, A.-C., Simcoe, R. A., et al. 2024, ApJ, 966, 176